



Ni-, Pt- and (Ni/Pt)-doped TiO₂ nanophotocatalysts: A smart approach for sustainable degradation of Rhodamine B dye



Roberto Pol^a, Miguel Guerrero^{b,*}, Eva García-Lecina^c, Ainhoa Altube^c, Emma Rossinyol^d, Sebastiano Garroni^e, Maria Dolors Baró^b, Josefina Pons^a, Jordi Sort^{f,*}, Eva Pellicer^b

^a Departament de Química, Facultat de Ciències, Universitat Autònoma de Barcelona, E-08193 Bellaterra, Spain

^b Departament de Física, Facultat de Ciències, Universitat Autònoma de Barcelona, E-08193 Bellaterra, Spain

^c Surfaces Division, IK4-CIDETEC, Paseo Miramón, 196, E-20009 San Sebastián, Spain

^d Servei de Microscòpia, Universitat Autònoma de Barcelona, E-08193 Bellaterra, Spain

^e Dipartimento di Chimica e Farmacia, Università di Sassari and INSTM, Via Vienna 2, I-07100 Sassari, Italy

^f Institució Catalana de Recerca i Estudis Avançats (ICREA) and Departament de Física, Universitat Autònoma de Barcelona, E-08193 Bellaterra, Spain

ARTICLE INFO

Article history:

Received 8 May 2015

Received in revised form 28 July 2015

Accepted 4 August 2015

Available online 6 August 2015

Keywords:

Photocatalyst

Nanoporosity

Titania

Magnetic properties

Water remediation

ABSTRACT

Ni (1 wt%)-, Pt (1 wt%)- and [Ni (0.5 wt%)/Pt (0.5 wt%)]-doped TiO₂ nanoporous catalysts have been successfully obtained through a facile two-step hydrothermal route. TiO₂ crystallizes mostly in the anatase phase and acts as a mesoporous matrix. Meanwhile, Ni, Pt and Ni/Pt dopants form small nanoparticles (NPs) (3–95 nm in diameter) which are hosted by the TiO₂ framework. The resulting composites exhibit a rather large surface area, in the range of 186–200 m²/g. The band gap energy reduces from 3.03 eV for the undoped TiO₂ to 2.15 eV for the Pt-loaded TiO₂. As a consequence, absorption expands toward the visible light range. The photodegradation of Rhodamine B dye in aqueous medium has been investigated under UV–vis light irradiation. The presence of Ni, Pt and Ni/Pt NPs significantly enhances the photocatalytic activity of the material. Furthermore, the Ni-doped TiO₂ shows ferromagnetic behavior at room temperature, which makes its recovery and subsequent fast reutilization possible. Interestingly, this sample also exhibits the best stability upon recycling. Considering all the current challenges in sustainable water remediation, these new photocatalysts could find applications in real environmental contexts in the near future.

© 2015 Elsevier B.V. All rights reserved.

1. Introduction

Large amounts of water are currently used in several cleaning and staining processes. Modern industrial activities have left wide-spread hazardous pollution in soil and water across the globe

Abbreviations: NPs, nanoparticles; POPs, persistent organic pollutants; HPO, heterogeneous photocatalytic oxidation; TM, transition metal; HPT, highly porous TiO₂; HRTEM, high resolution transmission electron microscopy; EDX, energy dispersive X-ray; SEM, scanning electron microscopy; XRD, X-ray diffraction; MAUD, materials analysis using diffraction; BET, Brunauer–Emmett–Teller; BJH, Barrett–Joyner–Halenda; VSM, vibrating sample magnetometer; ICP-OES, inductively coupled plasma–optical emission spectroscopy; RhB, rhodamine B; UV, ultraviolet; Vis, visible; JCPDS, joint committee on powder diffraction standards; fcc, face-centered cubic; S_{bet}, BET surface area; SAED, selected area electron diffraction; MS, saturation magnetization; DRS, diffuse reflectance spectra; VB, valence band; CB, conduction band; BG, band gap.

* Corresponding authors.

E-mail addresses: Miguel.Guerrero@uab.cat (M. Guerrero), Jordi.Sort@uab.cat (J. Sort).

<http://dx.doi.org/10.1016/j.apcatb.2015.08.006>

0926-3373/© 2015 Elsevier B.V. All rights reserved.

[1]. One of the most troublesome groups of pollutants is persistent organic pollutants (POPs) like dyes, detergents or pesticides due to their water solubility and chemical stability [2–4]. The presence of these colored compounds in the environment causes considerable non-aesthetic pollution and serious health-risk issues [5]. Since conventional wastewater treatments cannot eliminate the majority of these pollutants, powerful methods for the decontamination of dye wastewaters have received increasing attention over the last decade. Ozonation and electrocoagulation are among these methods. However, they consist of multiple steps and are rather costly and time-consuming [6].

Aqueous heterogeneous photocatalytic oxidation (HPO) is considered as one of the greener and cheaper approaches for the removal of POPs. HPO consists in the acceleration of a photoreaction in the presence of a catalyst in water [7]. In other words, it combines water as a green and abundant resource with solar light as an affordable, renewable and clean energy source. HPO involves the breakdown of pollutants into harmless substances while avoiding residues or additional sludge. For these reasons, HPO has received

special attention for remediating global water pollution and it is moving fast from the laboratory scale to industrial applications [8,9].

TiO₂ is one of the most studied, environmentally-friendly, photocatalytic materials due to its chemical stability, low toxicity, and light conversion efficiency [10]. Despite these advantages, TiO₂ presents the drawback of limited photocatalytic activity because of its wide band gap (3.2 eV for anatase phase). Therefore, it requires excitation wavelength in the UV domain ($\lambda < 390$ nm), which limits its practical efficiency. One of the most common approaches to expand the TiO₂ response toward the visible light domain is through doping it with suitable anions (e.g. N, C, S) or cations and transition metal (TM) clusters or nanoparticles (NPs) [11,12].

The controlled doping of TiO₂ with TM species has been the object of several investigations. An enhancement of the catalytic activity of TiO₂ in a number of manifold reactions has been ascribed to the effects induced by the TM at various levels. For example, Mn-Ni doped TiO₂ catalysts showed increased NO reduction to N₂ and offered the possibility to widen the temperature window of the reaction [13]. Also, Nb-doped TiO₂ particles have been studied as electrocatalysts for the oxygen reduction reaction under acidic conditions [14].

Among the TMNPs available to be dispersed on high-surface area TiO₂ for photocatalytic purposes, those made of Pt hold a privileged position [15–17]. In general, the resulting nanocomposite benefits from the catalytic activity of the TMNPs and the intrinsic photocatalytic activity of TiO₂. If the TMNPs possess magnetic properties (e.g. Ni, Co, Fe), then recovery and recycling of the catalyst becomes feasible under the application of a magnetic field. This poses some advantages compared to cross-flow filtration or centrifugation processes [18], since the recovery of a catalyst using magnetic fields is much cheaper and faster.

In this work, nickel, platinum and nickel/platinum-doped TiO₂ porous nanophotocatalysts have been successfully obtained through “an” easy two-step hydrothermal route. The morphology, crystallographic structure of the composite constituents, and eventual magnetic properties of the material have been investigated. Furthermore, the degradation kinetics of Rhodamine B (RhB) dye under ultraviolet-visible light irradiation has been assessed. RhB is one of the most common xanthene dyes used as a colorant in the textile industry. It is highly water soluble and presents a good stability as dye laser material. Nowadays, its use has been forbidden due to its potentially toxic and carcinogenic properties. Thus, the photodegradation of this organic compound is important with regard to the purification of dye effluents.

2. Materials and methods

2.1. Sample preparation

All chemicals were commercially available and used without further purification. Titanium (IV) butoxide (97%), 1-butanol (99.9%), nitric acid (69%), chloroplatinic acid hexahydrate (H₂PtCl₆·6H₂O) (37.5% Pt basis) and nickel (II) nitrate hexahydrate (Ni(NO₃)₂·6H₂O) (20.19% Ni basis) were purchased from Sigma Aldrich. Pluronic P123 was provided by BASF.

Highly porous TiO₂ (denoted as ‘HPT’) sample was prepared by sol-gel hydrothermal method. First, 7 mL of titanium butoxide (VI) dissolved in 40 mL of 1-butanol was added dropwise to 60 mL of distilled water at pH = 2 (adjusted with nitric acid). After continuous stirring of the reaction mixture for 20 h, the resultant suspension was subjected to a hydrothermal treatment in a plastic flask at 80 °C for 2 h. Afterwards, 2.5 g of Pluronic P123 triblock copolymer was dissolved in 40 mL of distilled water and the solution was added dropwise to the titanium (VI) butoxide solution, which had been

previously cooled down to 45 °C. Then the mixture was stirred at this temperature for 2 h followed by a second hydrothermal treatment in a plastic flask at 80 °C for 20 h. The resultant powder was recovered by evaporation at 60 °C. Finally, the titania product was obtained by calcination in a furnace at 450 °C for 4 h in air, by which the P123 was also removed.

Nickel, platinum and nickel/platinum-doped TiO₂ (denoted as ‘Ni/HPT’, ‘Pt/HPT’ and ‘Ni/Pt/HPT’, respectively) were prepared following a similar procedure to that of pure TiO₂. A P123-titanium (VI) butoxide mixture was obtained as described above prior to the doping step. To dope TiO₂ with Ni, Pt and bimetallic Ni/Pt NPs, a solution containing the metal salts (nickel (II) nitrate hexahydrate, chloroplatinic acid hexahydrate or chloroplatinic acid hexahydrate + nickel (II) nitrate hexahydrate) in 10 mL of distilled water was added dropwise to the P123-titanium (VI) butoxide mixture at 80 °C. Unless otherwise stated, the loading amounts were 1 wt% for both Ni/HPT and Pt/HPT samples and 0.5 wt%/0.5 wt% for the Ni/Pt/HPT sample. The mixture was subjected to 30 min sonication in order to achieve good dispersion of the precursors. The resultant powder was recovered by evaporation at 60 °C. This was followed by a thermal treatment in a furnace at 450 °C under H₂ atmosphere for 4 h in order to obtain the doped nanocomposites.

2.2. Characterization

High resolution transmission electron microscopy (HRTEM) was performed on a Jeol-JEM 2011 system operated at 200 kV and equipped with energy dispersive X-ray (EDX) detector. Scanning electron microscopy (SEM) observations were done using a Merlin Zeiss microscope operated at 2 kV. Samples for HRTEM were prepared by dispersing a small amount of powder in ethanol (96%) followed by sonication. A holey carbon grid was then soaked into the suspension and allowed to dry in air. The size distribution of Ni and Pt NPs was determined via manual analysis of enlarged micrographs. Around 100 particles were counted in order to obtain statically meaningful size distributions and the mean diameter. Wide-angle X-ray diffraction (XRD) patterns were collected on a Philips X’Pert diffractometer in the 20–80° 2 θ range (step size = 0.03°, step time = 10 s) using CuK α radiation. The structural parameters (phase percentage, crystallite size and cell parameters) were determined using the “Materials Analysis Using Diffraction” (MAUD) Rietveld refinement software [19,20].

N₂ sorption isotherms were measured on a Sorptomatic 1990 and the data were analyzed according to Brunauer-Emmett-Teller (BET) and Barrett-Joyner-Halenda (BJH) methods [21]. Around 800 mg of powder were charged in a quartz tube and then degassed under high vacuum (1×10^{-3} bar) at 250 °C for 24 h to remove the solvent. Room temperature hysteresis loops were collected using a vibrating sample magnetometer (VSM) from Oxford Instruments, with a maximum applied magnetic field of 1 T. Inductively coupled plasma–optical emission spectroscopy (ICP-OES) was carried out on a PerkinElmer Optima 4300DV model. 2–5 mg of powder were digested in aqua regia and concentrated hydrofluoric acid (HF) solution at 200 °C for 8–10 min on a CEM model MARS microwave oven.

2.3. Evaluation of photocatalytic activity

The photocatalytic activity of the powder samples was evaluated by decolorization of a 10 ppm RhB aqueous solution (Alfa Aesar, 98%, used without further treatment). Solutions were prepared by adding 0.3 g L⁻¹ of the catalyst to 10 mL of the RhB solution. A blank RhB solution (without catalyst) was used as a control test. The reaction cells were placed in a SwiftCure IB irradiation cabin equipped with a mercury lamp. Suitable cut-off filters were used to limit the wavelength radiation and avoid direct photolysis of

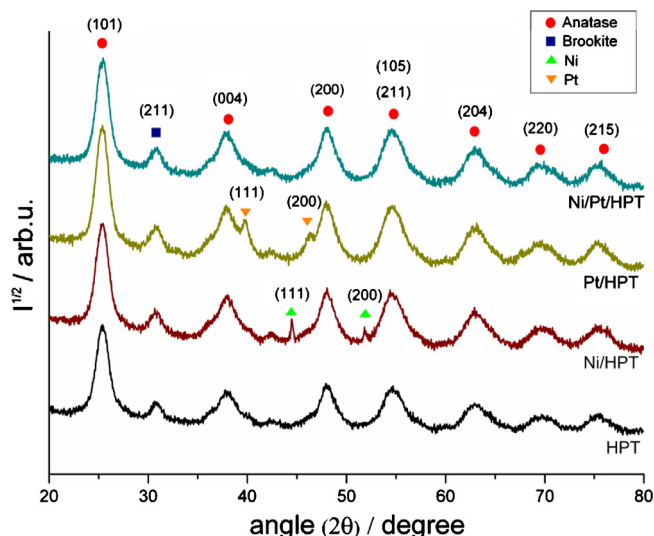


Fig. 1. XRD data of HPT, Ni/HPT, Pt/HPT and Pt/Ni/HPT samples.

the dye (ISO 10678:2010 standard). The average light intensity used was 220 W and the wavelength ranged from 300 to 500 nm, thus covering part of ultraviolet (UV) (300–400 nm) and visible (Vis) (400–700 nm) regions. The photocatalytic experiments were conducted under continuous magnetic stirring at a constant temperature of 25 °C.

Aliquots were withdrawn regularly at time intervals of 0, 15, 30, 60, 120, and 180 min from the reaction. The supernatant solutions were then tested with a UV–vis spectrophotometer (Shimadzu UV-1603) by measuring absorption spectra of RhB ($\lambda = 554$ nm) as a function of the irradiation time. Photocatalytic activity of the catalysts was calculated as (C/C_0) , where C_0 is the absorbance of the test solution of RhB before irradiation and C is the absorbance of RhB after irradiation. The optical diffuse reflectance spectra were measured at room temperature using the same UV–vis instrument equipped with an integrating sphere attachment and using NaF as reference. In order to investigate the reusability of the photocatalysts, five consecutive cycles were conducted. After each cycle, the photocatalytic material was centrifuged, collected and dispersed in a fresh RhB aqueous solution.

3. Results and discussion

3.1. Morphological and structural characterization

In Scheme 1 the synthesis route toward HPT, Ni/HPT, Pt/HPT and Ni/Pt/HPT samples is presented. The total dopant metal amount was kept at 1 wt% in the synthesis. The actual Pt and Ni amounts determined by ICP-OES are shown in Supplementary data (Table S1). The results indicate that there is no significant difference between the nominal and the actual dopant metal percentage in the nanocomposites.

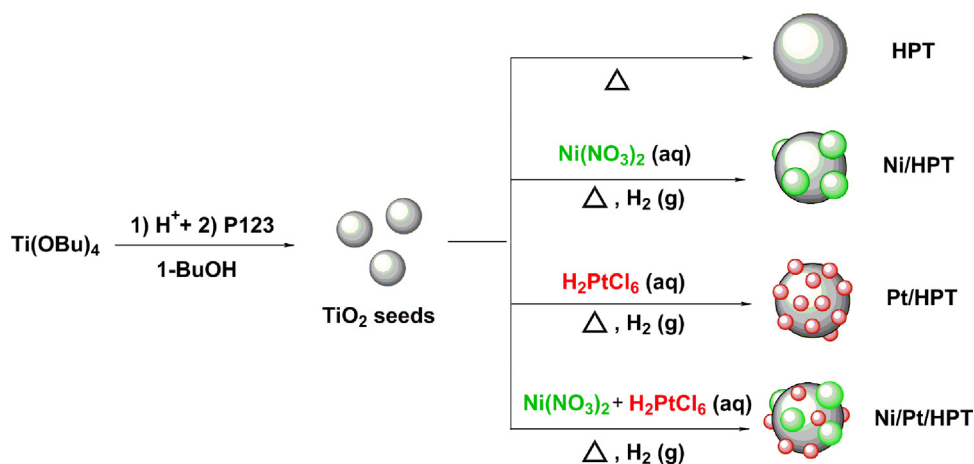
The crystallographic structure of the different samples was studied by XRD (Fig. 1). Broad reflections ascribed to TiO_2 were observed for all samples, indicating its nanocrystalline nature. The most predominant phase in the diffractogram of non-doped TiO_2 sample (HPT) is anatase (tetragonal phase) (JCPDS no. 84-1286). Namely, the peaks at 25.3°, 37.8° and 48.0° correspond to the (1 0 1), (0 0 4) and (2 0 0) crystal planes, respectively, of TiO_2 -anatase structure. The brookite phase is also present, as revealed by the characteristic reflection of (2 1 1) at $2\theta = 30.7^\circ$. Besides the characteristic diffraction peaks of anatase and brookite phases, the diffractogram of Ni-doped TiO_2 sample (Ni/HPT) exhibits two reflections at 44.6°

and 52.0° that match the positions of (1 1 1) and (2 0 0), respectively, of face-centered cubic (fcc) Ni. Likewise, the diffractogram of Pt-doped TiO_2 (Pt/HPT) shows two reflections at 39.6° and 46.2° ascribed to (1 1 1) and (2 0 0) planes, respectively, of fcc Pt. The bi-doped sample (Ni/Pt/HPT) does not present any reflections ascribed to Ni and/or Pt due to the lower amounts of both dopant metals (0.5 wt%), which fall below the sensitivity limit of the XRD technique (1–2 wt%).

Anatase and brookite phase percentages, as determined by Rietveld refinement of the full XRD patterns, as well as the cell parameter values and average crystallite size for anatase phase are listed in Table S2. All samples show lower c parameter than that of tabulated anatase (9.513 Å, JCPDS no. 84-1286). This could be attributed to the occurrence of unit cell shrinkage during the calcination process. Several factors like titania precursor [22], synthetic method [23] and calcination conditions [24] are known to determine the TiO_2 phase –rutile, anatase or brookite– and their relative proportion. Besides, samples show an average crystallite size in the range of 10–12 nm, in agreement with previous reports [25–28].

Fig. 2 shows the N_2 adsorption–desorption isotherms and the pore size distributions of all samples. A type IV isotherm characteristic of mesoporous materials is observed in all cases [29]. The adsorption branch exhibits three distinct regions corresponding to a monolayer-multilayer adsorption, multilayer adsorption on the outer particle surfaces and capillary condensation at relative pressures in the range from 0.6 to 0.9, for all the isotherms. H2-type hysteresis loop is observed, typical of samples with ink-bottle shaped pores and interconnecting channels. The powders showed a BET surface area (S_{bet}) of 186–200 m^2/g , with no significant differences among non-doped and doped TiO_2 , in agreement with the results of Di Paola et al. [30] (Table 1). Either unimodal or bimodal pore size distributions (Fig. 2, insets), with a maximum pore diameter between 7.8 and 10.9 nm and a cumulative pore volume between 0.456 and 0.572 cm^3/g , were obtained, similar to the values reported by E. Masolo et al. [31]. A narrower pore distribution was noticed for Pt/HPT sample (Fig. 2c, inset). It is conjectured that the narrower pore distribution in the Pt/HPT sample is mainly due to the very small size of the nucleated Pt NPs in comparison to that of the Ni ones (3 nm vs. 95 nm as it will be shown later). TiO_2 matrix formation is probably less disturbed when smaller NPs are accommodated within the network. As a result, the formation of the TiO_2 matrix becomes less perturbed when Pt is present and a narrower pore distribution is achieved. Interestingly, all doped samples exhibit a higher average pore diameter than non-doped TiO_2 sample.

To gain further structural information on the samples, TEM and HRTEM analyses were performed. HPT is highly porous and crystalline (Fig. 3a and b). The corresponding selected area electron diffraction (SAED) pattern (Fig. 3c) shows continuous rings indicating the existence of tiny crystals. Indexing of the primary rings is consistent with the existence of anatase ((1 0 1), (0 0 4) and (2 0 0) crystal planes) and brookite phases ((2 1 1) reflection) in agreement with XRD results. The most intense ring corresponds to an interplanar distance of 3.5 Å, which matches the d spacing of (1 0 1) anatase. HRTEM images of Ni/HPT and Pt/HPT nanocomposites (Fig. 3d and e) show well dispersed Ni and Pt rounded NPs, respectively. The average size of the Ni NPs in Ni/HPT sample is much larger than that of Pt NPs in Pt/HPT sample (95 nm and 3 nm, respectively) (Fig. S1). This difference in size could originate from the ability of Pt and Ni precursors to diffuse along the TiO_2 walls being formed. Although no bibliographic data of diffusion coefficients for Pt and Ni cations onto TiO_2 surfaces exist, it is believed that the coefficient diffusion of Ni cation is higher than that of Pt cation. The higher the diffusion coefficient, the easier the atoms can diffuse onto the TiO_2 to ultimately give rise to NPs of larger size. The inset in Fig. 3d shows a SAED pattern of the Ni/HPT sample focused on a Ni NP, in which it is



Scheme 1. Synthesis of undoped TiO₂ (HPT) and Ni-, Pt- and Ni/Pt-doped TiO₂ nanophotocatalysts (Ni/HPT, Pt/HPT and Ni/Pt/HPT, respectively).

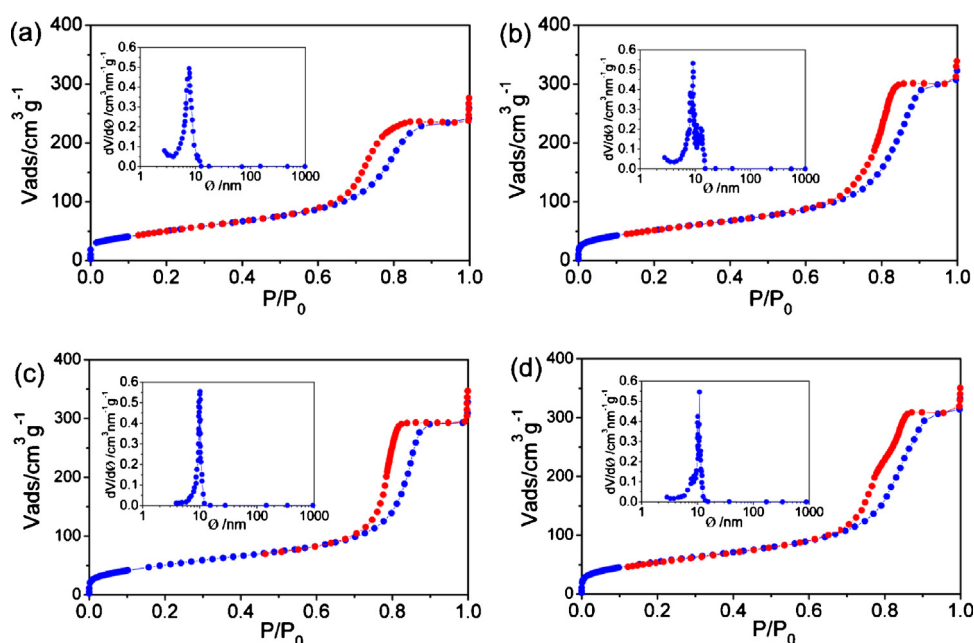


Fig. 2. N₂ adsorption (blue dots)-desorption (red dots) isotherms of (a) HPT, (b) Ni/HPT, (c) Pt/HPT and (d) Ni/Pt/HPT samples and their respective pore size distributions (insets). (For interpretation of the references to color in this figure legend, the reader is referred to the web version of this article.)

possible to distinguish a clear diffraction spot array whose d spacing is 2.02 Å. Such d spacing corresponds to (1 1 1) fcc Ni, which appears superimposed to the lattice rings of anatase. Interestingly, Ni and Pt NPs are also well dispersed in the bi-doped Ni/Pt/HPT nanocomposite (Fig. 3f). Notice that Ni and Pt do not form a core-shell structure or an alloy but rather they have nucleated independently, rendering individual single-phase NPs.

SEM imaging was used to study the surface morphology as well as the porosity of the different nanocomposites. Fig. 4 shows SEM

secondary electron images taken at different magnifications of the HPT sample, for which a large porosity is evident, in concordance with BET analyses. Porosity was preserved in the doped HPT samples (e.g. Ni/HPT in Fig. S2).

3.2. Magnetic and optical properties

The magnetic properties of the Ni-containing catalysts (i.e., Ni/HPT and Ni/Pt/HPT) were investigated using a vibrating

Table 1

Textural parameters determined by BET of HPT, Ni/HPT, Pt/HPT and Ni/Pt/HPT powders.

Samples	S_{bet} (± 5 m ² /g)	Maximum pore diameter (± 0.2 nm)	Average pore diameter (± 0.2 nm)	Micropore volume (± 0.002 cm ³ /g)	Cumulative pore volume (± 0.005 cm ³ /g)
HPT	186	7.8	7.8	0.067	0.456
Ni/HPT	200	9.2	9.6	0.075	0.572
Pt/HPT	187	10.2	9.9	0.066	0.558
Ni/Pt/HPT	191	10.7	10.0	0.069	0.556

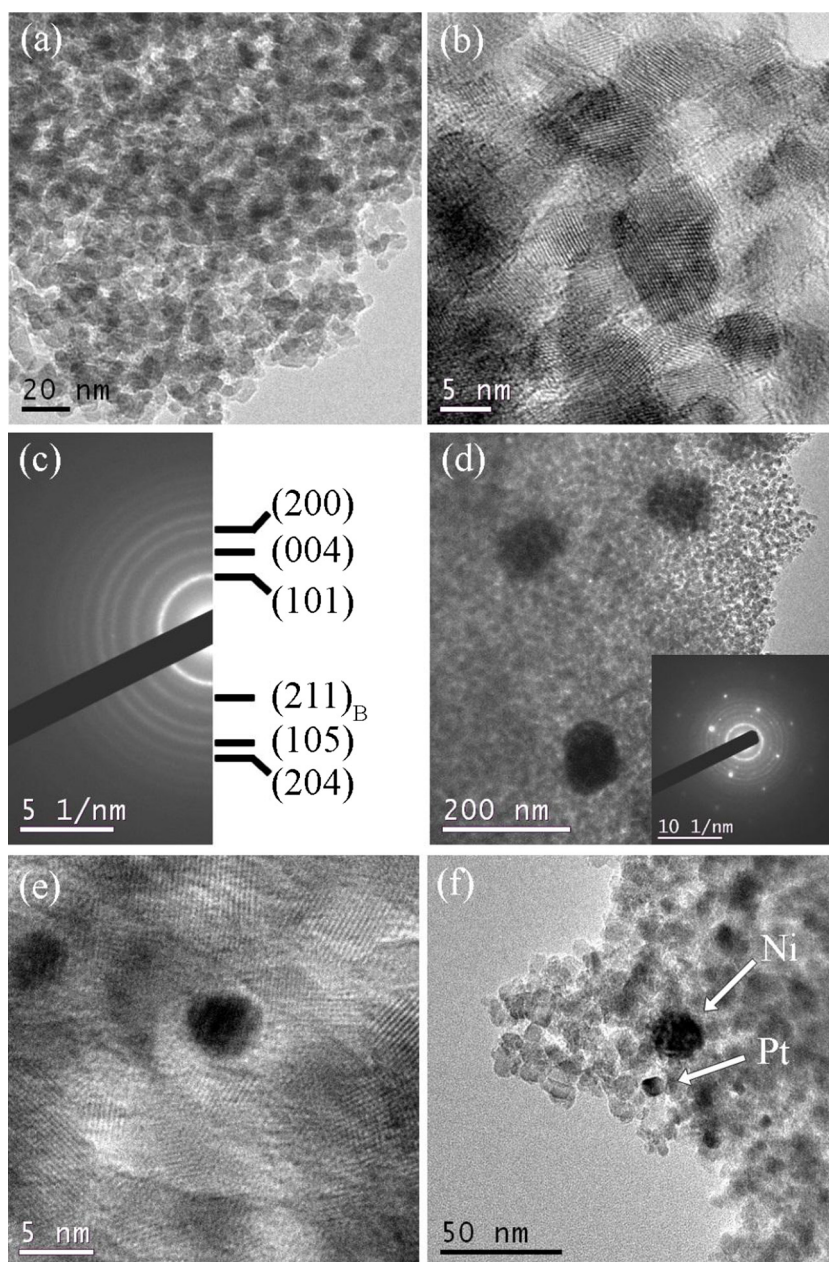


Fig. 3. TEM and HRTEM images of (a, b) HPT at different magnifications and (c) the corresponding SAED pattern; B means brookite phase. (d) TEM image of Ni/HPT (the SAED is shown in the inset), (e) HRTEM image of Pt/HPT, (f) TEM image of Ni/Pt/HPT.

sample magnetometer at room temperature (Fig. 5). The Ni/HPT sample exhibits a saturation magnetization (M_s) of 0.4 emu g^{-1} and a coercivity of around 80 Oe. Interestingly, although the M_s of the Ni/HPT powder is not high, it is large enough for the powder to become attracted by a circular NdFeB magnet (2500 Oe) of about 1 cm in diameter when it is brought near the sample (inset of Fig. 5). Almost all photocatalyst (99 wt%) is recovered after each photocatalytic cycle using this magnetic separation procedure, as verified from values of sample weight before and after the RhB degradation process. On the other hand, the Ni/Pt/HPT sample does not show a ferromagnetic behavior (i.e., no clear hysteresis loop).

UV–vis diffuse reflectance spectra (DRS) were carried out prior to the assessment of the photo-degradability performance of each catalyst. It is known that the optical properties of a photocatalyst and its catalytic performance are closely related [32]. HPT sam-

ple presents strong absorption only at wavelengths below 400 nm. Therefore, it shows photoabsorption only in the UV domain (Fig. 6). On the other hand, the spectra of doped samples (Ni/HPT, Pt/HPT and Ni/Pt/HPT) show a similar response in the UV domain and also absorption within the visible domain. In other words, the absorption spectrum expands into the visible range. This result can be attributed to the excitation of 3d (for Ni) and/or 5d (for Pt) electrons from the transition metal valence band (VB) to the TiO_2 conduction band (CB) [33].

The band gap (BG) energies (Table 2) were determined using the equation:

$$E_g = hc_0/\lambda_g \quad (1)$$

where E_g is the energy of the band gap in eV, h is the Planck's constant ($6.626 \times 10^{-34} \text{ Js}$), C_0 is the speed of light in vacuum ($3 \times 10^8 \text{ m/s}$) and λ_g is the value obtained measuring the inter-

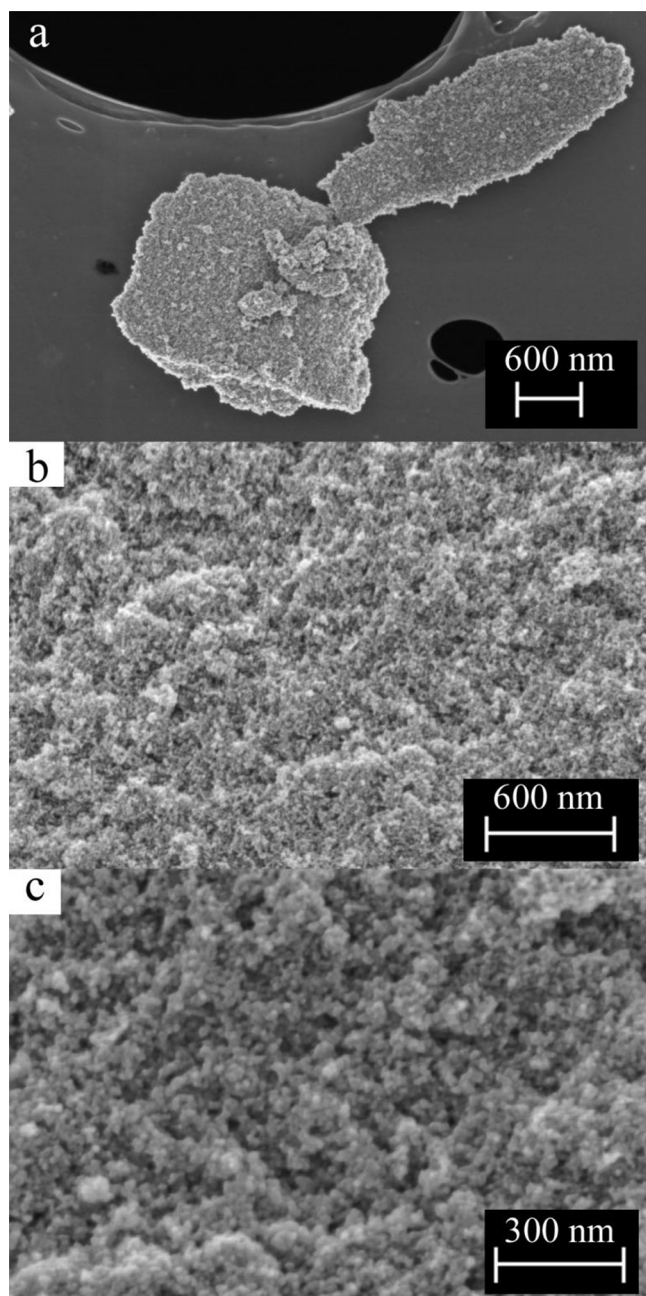


Fig. 4. (a–c) On-top SEM images at different magnification of the non-doped HPT sample.

section of the tangent of the absorption edge with the x -axis [34]. The absorption edge of HPT was noted at 408 nm, corresponding to a BG energy value of 3.03 eV. Conversely, Pt/HPT and Ni/HPT and Ni/Pt/HPT nanocomposites all possess smaller BG values (2.69–2.15 eV, Table 2).

Table 2
Calculated band gap energies and rate constant values for the different samples.

Samples	E_g (eV)	k (min^{-1})
HPT	3.03	0.0027
Ni/HPT	2.54	0.0046
Pt/HPT	2.15	0.0053
Ni/Pt/HPT	2.69	0.0041

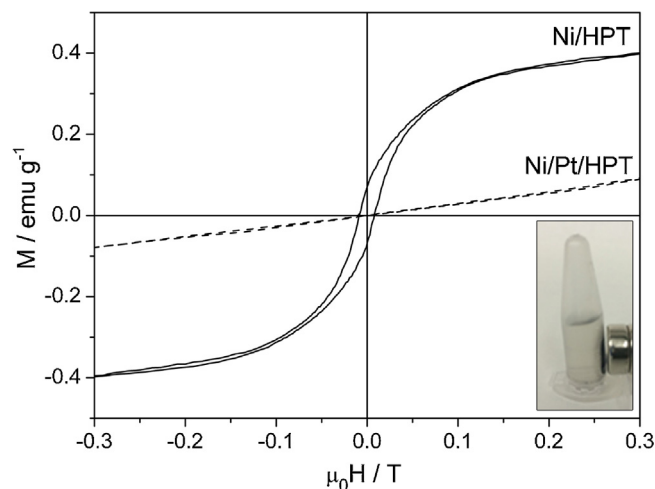


Fig. 5. Room-temperature magnetic hysteresis loops of Ni/HPT and Ni/Pt/HPT samples.

3.3. Photocatalytic activity

The photocatalytic performances of the catalysts were investigated by following the decomposition of RhB in an aqueous solution under irradiation with a mercury lamp (320–500 nm). No significant degradation of RhB was observed in the absence of any photocatalyst, which was taken as a reference (blank).

As shown in Fig. 7a, the concentration of RhB decreases linearly with time in the presence of the HPT sample, reaching a removal ratio of 39% after exposure for 180 min. The removal ratio of Pt/HPT, Ni/HPT and Ni/Pt/HPT were 63, 57 and 54%, respectively. The results show that there is an enhancement in the photodegradability of RhB when Ni or Pt NPs (or combinations of both) are loaded into TiO_2 . Previous works in the literature indicate that the photocatalytic oxidation of different dyes using TiO_2 as a catalyst follow the Langmuir-Hinshelwood kinetics model [35–37]. For very diluted catalyst suspensions (millimolar), though, the reaction can be described as a pseudo-first-order equation. This applies to our case (Fig. 7b), for which the $\ln(C/C_0)$ versus time follows a linear relationship. The slope corresponds to the apparent first-order rate constant (k , min^{-1}). The rate constants values (Table 2) show that Ni- and Pt-doped nanocomposites outperform HPT sample. Pt/HPT, with a BG energy value of 2.15 eV, presents the highest rate con-

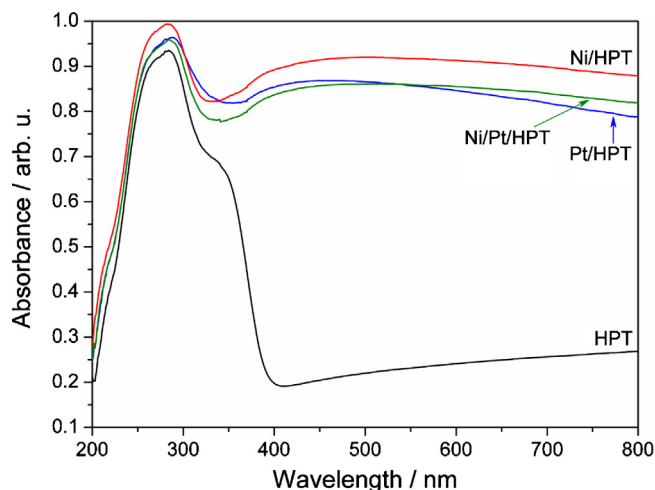


Fig. 6. UV-vis absorption spectra of HPT, Ni/HPT, Pt/HPT and Ni/Pt/HPT samples.

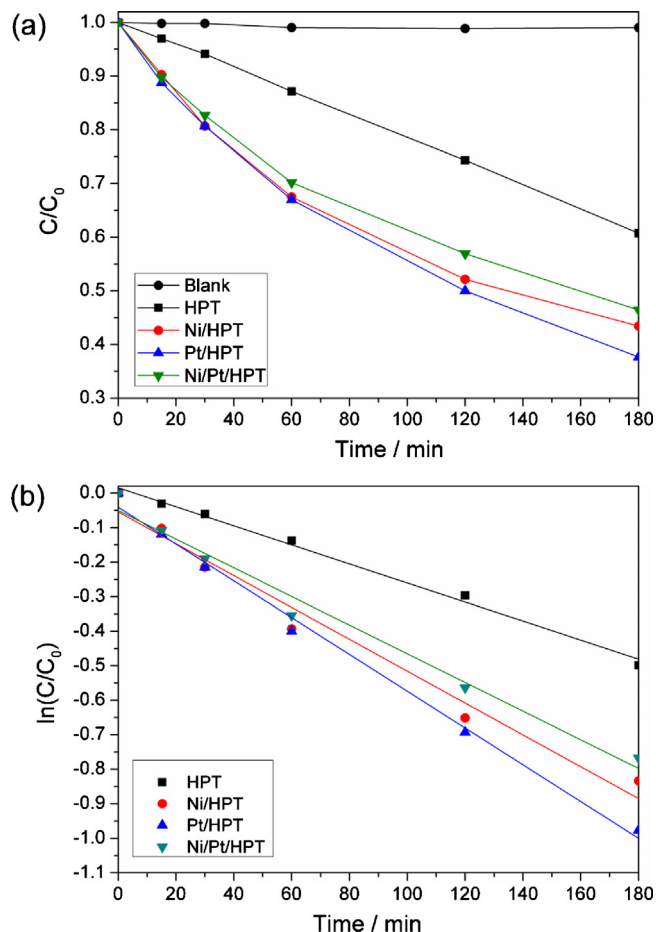


Fig. 7. (a) C/C_0 vs time plot showing the decrease of the dye concentration. (b) $\ln(C/C_0)$ of RhB vs time.

stant, 0.0053 min^{-1} . Meanwhile, Ni/HPT sample shows a slightly lower k value (0.0046 min^{-1}). Curiously, the corresponding k value for the bi-doped sample is lower than those of the single-doped TiO_2 catalysts. In spite of it, it is envisaged that having two different types of NPs physically separated but in the same support can be advantageous in certain cases. For example, two different reactions could be simultaneously catalyzed by taking advantage of the joint presence of Pt and Ni in the matrix. The rate constant of Pt/HPT sample is higher than that observed in the degradation of RhB using core(metal)-shell(TiO_2) nanocomposites (e.g. Pt, $k = 0.0013 \text{ min}^{-1}$) synthesized via a hydrothermal treatment with noble metal colloid particles [38]. Our results are also in good agreement with those previously reported by Chen et al. [39], who also observed an increase in the rate constant toward the degradation of *o*-cresol upon doping TiO_2 with Pt.

In order to further explore the influence of the dopant metal concentration on the photodegradation of RhB, two additional samples were prepared: Ni(3 wt%)/HPT and Pt(3 wt%)/HPT. The Ni and Pt particle size distributions are shown in Fig. S1. Notice that the average particle size is in both cases reduced as compared to the 1 wt% concentration. Additionally, the corresponding XRD patterns are also shown in Fig. S3. The RhB removal ratio of Ni(3 wt%)/HPT and Pt(3 wt%)/HPT were 39 and 38%, respectively, almost the same removal ratio of non-doped HPT sample (Fig. S4). Accordingly, there is a decrease of the photocatalytic efficiency when the concentration of dopant is exceedingly large. This can be explained by taking two scenarios into account: (1) the TMNNPs excess at the surface of TiO_2 decrease the charge carrier space distance (CCSD) via efficiently trapping photoelectrons and therefore increase recom-

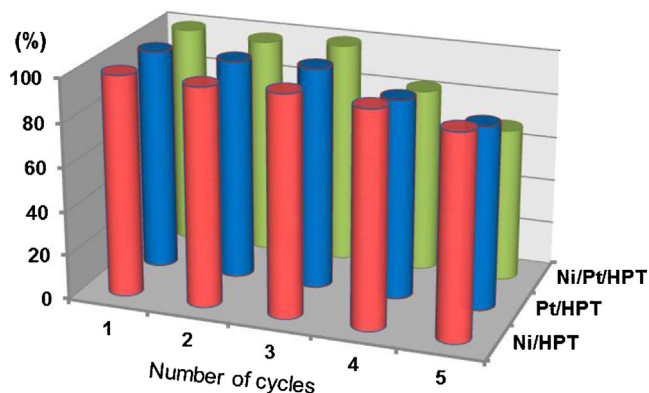


Fig. 8. Relative RhB degradation as a function of the number of cycles. (For interpretation of the references to color in the text, the reader is referred to the web version of this article.)

bination [40]; (2) a fraction of the active sites become 'covered' or 'shaded' so that the available space on the semiconductor for pollutant adsorption and light absorption is decreased, thereby reducing photodegradation efficiency [41]. Our results are in agreement with those of Dhabbe et al. [42] and Arabatzis et al. [43]. The former observed an enhancement of the photocatalytic performance upon increasing the content of Ag in N-doped TiO_2 nanocomposites until a maximum loading of 1 g/dm^3 . The latter pointed out an enhancement of the photocatalytic performance toward methyl orange degradation with an increase of the Au content in TiO_2 thin films till a maximum of $0.8 \mu\text{g/cm}^2$. In both cases, the catalytic activity diminished with further increase of the dopant concentration. Nevertheless, it is worth noticing that the Ni(3 wt%)/HPT sample exhibits a higher M_S value (0.87 emu g^{-1}), as expected for a larger Ni amount. Therefore, in those cases where a larger M_S is required to recover the catalyst, this sample still has the potential to be used.

The recyclability of the doped TiO_2 nanocomposites was tested for 5 photodegradation cycles of 60 min each (Fig. 8). The results show that the photocatalytic activity begins to fairly decline in the fourth cycle. This effect could be due to the presence of radicals with high reduction potentials that might cause partial oxidation of the TMNNPs. It should be noted that the decrease of the photocatalytic activity is less pronounced in the Ni/HPT sample (Fig. 8, red), making it the most suitable catalyst in terms of reusability for the decomposition of POPs. The reason why Ni/HPT is more durable than Pt/HPT might arise from the distinct mean size of Ni and Pt NPs (95 nm and 3 nm, respectively). Even though Pt is less prone to oxidation, the size-dependence reactivity effect of the NPs cannot be ruled out. In the case of Pt a larger fraction of surface atoms would be exposed to the medium and, hence the photocatalytic activity would decline earlier for the Pt/HPT sample.

Regarding the mechanism (Fig. 9a) behind the decomposition of RhB under UV–vis irradiation, it is conjectured that an electron (e_{CB}^-) and a hole (h_{VB}^+) are produced (Fig. 9b,i). On the one hand, e_{CB}^- can reduce O_2 to form superoxide radical anion (Fig. 9b,ii). Simultaneously, h_{VB}^+ can oxidize H_2O to form hydroxyl radicals (Fig. 9b,iii). Finally, RhB mineralization occurs (Fig. 9b,iv). For optimum TMNNPs content and size (i.e. 1 wt%), reaction (ii) would be favored. In this case, the CCSD is thought to increase. The band gap energy is reduced and, as a consequence, the absorption band extends toward the visible light domain. The fact that the Pt/HPT outperforms Ni/HPT can be attributed to a higher electron affinity and suitable work function of Pt metal, so that a better contact with TiO_2 forms [40]. On the contrary, for exceedingly large contents, recombination of charge carriers competes with (ii) due to the

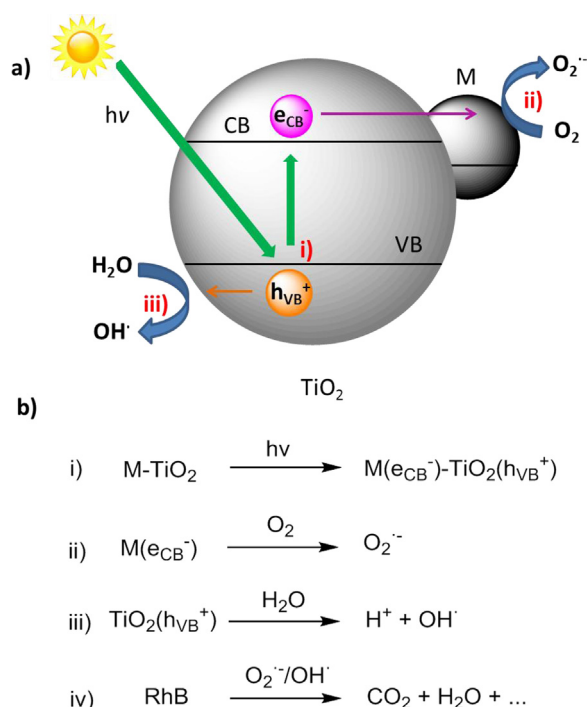


Fig. 9. Scheme of the proposed photochemical charge promoted separation.

decrease in the CCSD and/or the partial blocking of the available active sites for light absorption.

4. Conclusions

Ni-, Pt- and Ni/Pt-loaded TiO_2 nanophotocatalysts have been successfully prepared via a two-step hydrothermal route. The powders show a large porosity provided by the TiO_2 compound. The presence of Ni and Pt NPs within the TiO_2 matrix does not compromise the porosity, which remains large. TEM/HRTEM images reveal a homogenous distribution of the TMNPs within the sample powders, although the average NP size is different (that of Pt NPs is smaller). The photocatalytic activity of the nanocomposites outperforms that of non-doped TiO_2 synthesized following the same procedure. Higher degradation rates of Rhodamine B dye under UV–vis light irradiation are achieved (63% for Pt-, 57% for Ni and 54% for Ni/Pt-doped TiO_2 against 39% for undoped TiO_2). Furthermore, the Ni-doped TiO_2 sample presents sufficiently large M_5 values to allow its fast recovery from the media using relatively weak magnetic fields and subsequent reuse. The relative dye degradation keeps fairly constant up to the 4th cycle but starts to decrease onwards. Further work is in progress to elucidate the reasons behind such slight decrease in the photocatalytic activity, especially for the Pt-containing catalysts. Remarkably, an increase in the amount of loaded NPs does not bring an enhancement of the photocatalytic activity. Therefore, the tested dopant concentration (1 wt%) can be regarded as optimal. Considering the simplicity of the fabrication process and the attributes of these nanophotocatalysts, we expect that these materials could find uses in sustainable water remediation processes in the near future.

Author's contributions

The manuscript was written through contributions of all authors. All authors have given approval to the final version of the manuscript.

Notes

The authors declare no competing financial interest.

Acknowledgments

The authors sincerely thank BASF Corporation for kindly supplying the P123 precursor used for TiO_2 synthesis. The *Servei d'Anàlisi Química* and the *Servei de Difracció* from UAB are acknowledged. Financial support from the MAT2011-27380-C02-01, MAT2011-27380-C02-02, MAT2014-57960-C3-1-R and MAT2014-57960-C3-2-R research projects from the Spanish MINECO and the 2014-SGR-1015 project from the Generalitat de Catalunya are also acknowledged. E.P. acknowledges the Spanish *Ministerio de Economía y Competitividad* (MINECO) for the 'Ramón y Cajal' contract (RYC-2012-10839). M. Guerrero acknowledges the support of the Secretary for Universities and Research of the Government of Catalonia and the COFUND Programme of the Marie Curie Actions of the 7th R&D Framework Programme of the European Union for the 'Beatriu de Pinós' contract (2013 BP-B 00077). S. G. acknowledges "Fondazione Banco di Sardegna" for the financial support.

Appendix A. Supplementary data

Supplementary data associated with this article can be found, in the online version, at <http://dx.doi.org/10.1016/j.apcatb.2015.08.006>.

References

- [1] M.R. Hoffmann, S.T. Martin, W. Choi, D.W. Bahnemann, *Chem. Rev.* 95 (1995) 69–96.
- [2] C.H. Walker, *Organic Pollutants: An Ecotoxicological Perspective*, CRC Press, 2001.
- [3] Y. Wang, C.S. Hong, *Water Res.* 34 (2000) 2791–2797.
- [4] D. Barceló, *Emerging Organic Pollutants in Waste Waters and Sludge*, Springer, 2005, 2015.
- [5] E. Forgacs, T. Cserhati, G. Oros, *Environ. Int.* 30 (2004) 953–971.
- [6] C.A. Martínez-Huitle, E. Brillas, *Appl. Catal. B: Environ.* 87 (2009) 105–145.
- [7] C. Martínez, S. Vilarino, M.I. Fernández, J. Faria, L. Canle, J.A. Santaballa, *Appl. Catal. B: Environ.* 142–143 (2013) 633–646.
- [8] S. Malato, P. Fernandez-Ibanez, M.I. Maldonado, J. Blanco, W. Gernjak, *Catal. Today* 147 (2009) 1–59.
- [9] A.O. Ibadon, P. Fitzpatrick, *Catalysts* 3 (2013) 189–218.
- [10] J. Schneider, M. Matsuoka, M. Takeuchi, J. Zhang, Y. Horiuchi, M. Anpo, D.W. Bahnemann, *Chem. Rev.* 114 (2014) 9919–9986.
- [11] N. Serpone, *J. Phys. Chem. B* 110 (2006) 24287–24293.
- [12] N. Nishiyama, Y. Fujiwara, K. Adachi, K. Inumaru, S. Yamazaki, *Appl. Catal. B: Environ.* 176–177 (2015) 347–353 <http://dx.doi.org/doi:10.1016/j.apcatb.2015.04.015>
- [13] B. Thirupathi, P.G. Smirniotis, *Appl. Catal. B: Environ.* 110 (2011) 195–206.
- [14] T. Arashi, J. Seo, K. Takanebe, J. Kubota, K. Domen, *Catal. Today* 233 (2014) 181–186.
- [15] J.J. Murcia, M.C. Hidalgo, J.A. Navío, J. Araña, J.M. Doña-Rodríguez, *Appl. Catal. B: Environ.* 150–151 (2014) 107–115.
- [16] B.D. Fraters, R. Amrollahi, G. Mul, *J. Catal.* 324 (2015) 119–126.
- [17] X. Wang, J.C. Yu, H.Y. Yip, L. Wu, P.K. Wong, S.Y. Lai, *Chem. Eur. J.* 11 (2005) 2997–3004.
- [18] S. Shylesh, W.R. Thiel, V. Schunemann, *Angew. Chem. Int. Ed.* 49 (2010) 3428–3459.
- [19] R.A. Young, *The Rietveld Method*, International Union of Crystallography, Oxford University Press, 1995.
- [20] D.L. Bish, J.E. Post, *Am. Mineral.* 78 (1993) 932–940.
- [21] K.S.W. Sing, D.H.R. Everett, A.W. Haul, L. Moscou, R.A. Pierotti, J. Rouquerol, T. Siemieniowska, *Pure Appl. Chem.* 57 (1985) 603–619.
- [22] Y. Liu, M. Aizawa, Z. Wang, H. Hatori, N. Uekawa, H. Kanoh, *J. Colloid Interface Sci.* 322 (2008) 497–504.
- [23] D.A.H. Hanaor, C.C. Sorrell, *J. Mater. Sci. Lett.* 46 (2011) 855–874.
- [24] M.A. Aramendia, V. Borau, J.C. Colmenares, A. Marinas, J.M. Marinas, J.A. Navío, F.J. Urbano, *Appl. Catal. B: Environ.* 80 (2008) 88–97.
- [25] N. Bahadur, R. Pasricha, Govind, S. Chand, R.K. Kotnala, *Mater. Chem. Phys.* 133 (2012) 471–479.
- [26] B. Rajamannan, S. Mugundan, G. Viruthagiri, N. Shanmugam, R. Gobi, P. Praveen, *Acta Mol. Biomol.* 128 (2014) 218–224.
- [27] B.K. Vijayan, N.M. Dimitrijevic, J. Wu, K.A. Gray, *J. Phys. Chem. C* 114 (2010) 21262–21269.

- [28] R.M. Mohameda, E.S. Aazama, J. Alloys Compd. 509 (2011) 10132–10138.
- [29] J.M. Thomas, W.J. Thomas, Principles and Practice of Heterogeneous Catalysis, VCH, 1997.
- [30] A. Di Paola, G. Marci, L. Palmisano, M. Schiavello, K. Uosaki, S. Ikeda, B. Ohtani, J. Phys. Chem. B 103 (2002) 637–645.
- [31] E. Masolo, M. Meloni, S. Garroni, G. Mulas, S. Enzo, M.D. Baró, E. Rossinyol, A. Rzesutek, I. Herrmann-Geppert, M. Pilo, Nanomaterials 4 (2014) 583–598.
- [32] M. Guerrero, A. Altube, E. García-Lecina, E. Rossinyol, M.D. Baró, E. Pellicer, J. Sort, ACS Appl. Mater. Interfaces 6 (2014) 14583–14589.
- [33] S. Wang, J.S. Lian, W.T. Zheng, Q. Jiang, Appl. Surf. Sci. 263 (2010) 260–265.
- [34] R. López, R. Gómez, J. Sol–Gel Sci. Technol. 61 (2012) 1–7.
- [35] G. Sivalingam, K. Nagaveni, M.S. Hegde, G. Madras, Appl. Catal. B: Environ. 45 (2003) 23–38.
- [36] Y. Li, X. Li, J. Li, J. Yin, Water Res. 40 (2006) 1119–1126.
- [37] C.G. da Silva, J.L. Faria, J. Photochem. Photobiol. A: Chem. 155 (2003) 133–143.
- [38] N. Zhang, S. Liu, X. Fu, Y. Xu, J. Phys. Chem. C 115 (2011) 9136–9145.
- [39] H. Chen, Y. Ku, Y. Kuo, Water Res. 41 (2007) 2069–2078.
- [40] S. Sakthivel, M.V. Shankar, M. Palanichamy, B. Arabindoo, D.W. Bahnemann, V. Murugesan, Water Res. 38 (2004) 3001–3008.
- [41] X. Liu, Z. Liu, J. Lu, X. Wu, B. Xu, W. Chu, Appl. Surf. Sci. 288 (2014) 513–517.
- [42] R.S. Dhabbe, A.N. Kadam, M.B. Suwarnkar, M.R. Kokate, K.M. Garadkar, J. Mater. Sci.: Mater. Electron. 25 (2014) 3179–3189.
- [43] I.M. Arabatzis, T. Stergiopoulos, D. Andreeva, S. Kitova, S.G. Neophytides, P. Falaras, J. Catal. 220 (2003) 127–135.